The Astrophysical Journal Letters, 899:L14 (7pp), 2020 August 10 https://doi.org/10.3847/2041-8213/aba905

Axial Asymmetry Studies in Gaia Data Release 2 Yield the Pattern Speed of the Galactic Bar

Austin Hinkel[1], Susan Gardner[1], and Brian Yanny[2]
[1] Department of Physics and Astronomy, University of Kentucky, Lexington, KY 40506-0055, USA
[2] Fermi National Accelerator Laboratory, Batavia, IL 60510, USA
Received 2020 June 17; revised 2020 July 22; accepted 2020 July 23; published 2020 August 10

Abstract

Our recent studies of axial-symmetry breaking in the nearby ($d < 3$ kpc) star counts are sensitive to the distortions of stellar orbits perpendicular and parallel to the orientation of the bar just within and beyond the outer Lindblad resonance (OLR) radius. Using the location of the sign flip in the left–right asymmetry in stars counts about the anticenter line to determine the OLR radius $R_{\rm OLR}$, and treating the bar as if it were a weakly nonaxisymmetric effect, we use $R_{\rm OLR}$ and recent measurements of the Galactic rotation curve and the Sun–Galactic-center distance R_0 to determine the pattern speed $\Omega_{\rm p}$ of the Galactic bar, as well as the Galactic corotation radius $R_{\rm CR}$. After removing the effect of the Large and Small Magellanic Clouds from our asymmetry measurement, we find that $R_{\rm OLR} = (0.96 \pm 0.03)R_0 = 7.85 \pm 0.25$ kpc, $\Omega_{\rm p} = 49.3 \pm 2.2\,{\rm km\,s^{-1}\,kpc^{-1}}$, $R_{\rm CR} = (0.58 \pm 0.04)R_0 = 4.76 \pm 0.27$ kpc, revealing, as we shall show, that the Milky Way's bar is likely both weak and fast, though we also note possible evidence for non-steady-state effects in the bar region.

Unified Astronomy Thesaurus concepts: Galactic bulge (2041); Galactic center (565); Milky Way dynamics (1051); Milky Way rotation (1059)

1. Introduction

It is well established that there is a bar at the center of the Galaxy (Gerhard & Wegg 2015) and that this structure rotates in a manner such that its stars and dust have net motion in the bar rest frame (Binney & Tremaine 2008). The pattern speed, $\Omega_{\rm p}$, is the assessment of this rotation of the bar's potential, and models of that unknown potential are ordinarily needed in order to explain the motion of certain stellar populations to infer properties of the bar. This theoretical barrier, along with observational issues associated with high source densities, extinction, and reddening in the central region of the Galaxy, have resulted in a wide array of values, differing by more than a factor of 2, for $\Omega_{\rm p}$ (Bland-Hawthorn & Gerhard 2016). To illustrate, various methods (Dehnen 2000; Debattista et al. 2002; Chakrabarty 2007; Minchev et al. 2007; Antoja et al. 2014) favor a fast bar, such as the pattern speed of $\Omega_{\rm p} = 57.4^{+2.8}_{-3.3}\,{\rm km\,s^{-1}\,kpc^{-1}}$ (Chakrabarty 2007), whereas studies in the Galactic bar region (Portail et al. 2015, 2017; Bovy et al. 2019; Sanders et al. 2019) can find considerably slower values, such as $\Omega_{\rm p} = 25$–$30\,{\rm km\,s^{-1}\,kpc^{-1}}$ (Portail et al. 2015). Bearing in mind the varied pictures and mechanisms employed in determining the pattern speed, the review of Bland-Hawthorn & Gerhard (2016) gives a recommended range of $\Omega_{\rm p} = 43 \pm 9\,{\rm km\,s^{-1}\,kpc^{-1}}$. A model-independent method of measuring the pattern speed that utilizes the continuity equation does exist, however, if the pattern is steady (Tremaine & Weinberg 1984; Debattista et al. 2002; Sanders et al. 2019), but implementing it requires proper motion information for stars in the Galactic bar. Recently Sanders et al. (2019) have used Gaia Data Release 2 (DR2) and VISTA Variables in the Via Lactea (VVV) data (Minniti et al. 2010) to find $\Omega_{\rm p} = 41 \pm 3\,{\rm km\,s^{-1}\,kpc^{-1}}$, where the error is statistical only, with an additional suggested systematic uncertainty of 5–$10\,{\rm km\,s^{-1}\,kpc^{-1}}$.

The wide range of reported pattern speeds is also partly responsible for the wide range of radii associated with resonant effects driven by the Galactic bar, that is, the radius of the Outer Lindblad resonance (OLR) and the radius of the corotation resonance (CR). As such, it is unclear whether the stellar streams seen in the solar vicinity (Raboud et al. 1998; Dehnen 1999; Fux 2001; Sellwood 2010) are due to a CR (e.g., Mishurov & Zenina 1999) or an OLR (e.g., Dehnen 2000) or a 4: 1 OLR (Hunt & Bovy 2018). Until recently (Hinkel et al. 2020), there has been no model-independent way of discriminating between the possibilities in the existing data.

This lack of consensus regarding the pattern speed may come, in part, from the use of astrometric/photometric methods (Debattista et al. 2002; Bovy et al. 2019; Sanders et al. 2019) or of dynamical methods (Englmaier & Gerhard 1999; Portail et al. 2015, 2017), and this spills over into the debate on the location of the resonances of the Galactic bar. Moreover, it has been suggested that the inconsistencies between the two sorts of methods can be reduced by having the bar rotate at a slower speed today than it has in the past (Monari et al. 2017). The findings of Sanders et al. (2019) may yield a simpler explanation: systematic effects from dust, e.g., tend to lower assessments of the pattern speed artificially, especially when observations of stars from the far side of the Galactic center (GC) are used. Namely, Sanders et al. (2019) find $\Omega_{\rm p} = 41 \pm 3\,{\rm km\,s^{-1}\,kpc^{-1}}$ and $\Omega_{\rm p} = 31 \pm 1\,{\rm km\,s^{-1}\,kpc^{-1}}$ for stars in the near side of the bar and in both the near and far sides, respectively, providing the basis for their systematic error assessment. Alternatively, Hilmi et al. (2020) suggest that the bar's length and pattern speed can fluctuate by as much as 20% as the bar interacts with nearby spiral arms, perhaps explaining the different estimates of $\Omega_{\rm p}$ from different methods. Hilmi et al. (2020) note that the pattern speed as inferred from outer disk dynamics should reveal the time-averaged value of $\Omega_{\rm p}$, as opposed to instantaneous values measured in the central region via astrometric or photometric methods.

For a given galactic rotation curve, the pattern speed sets where these resonances are located. Thus, the determination of a resonant radius can also be used to fix the pattern speed, with

information on additional resonant radii giving further information on the morphology of the bar. As motivated by leading-order perturbation theory in the strength of the nonaxisymmetric bar potential (Binney & Tremaine 2008), stars in resonant orbits between the inner Lindblad resonance (ILR) and the CR are oriented along the bar, stars between the CR and the OLR orbit with trajectories perpendicular to the bar, and beyond the OLR the stellar orbits tend to be elongated along the bar's orientation (Contopoulos & Papayannopoulos 1980). These features are expected to persist even as the bar potential grows strong, though the fractional number of stars following the particular orbits predicted by leading-order perturbation theory may grow small (Binney & Tremaine 2008). Nevertheless, by using the change in sign of the axial asymmetry in star counts (Gardner et al. 2020; Hinkel et al. 2020) to determine the location of the OLR and using leading-order perturbation theory to determine the pattern speed as well as the CR, we find that our determined CR is crudely commensurate with the length of the Galactic bar—this is expected if the Galaxy's bar is indeed weak (Aguerri et al. 1998).

In this Letter, we employ a novel, model-independent method for determining the bar's pattern speed and resonant effects by leveraging our ability to detect axially asymmetric orbits. From tests of axisymmetry of our galaxy (Gardner et al. 2020), Hinkel et al. (2020) determine the radius of the OLR using Gaia DR2 data (Prusti et al. 2016; Brown et al. 2018; Lindegren et al. 2018), and here we use this measurement along with leading-order perturbation theory (Binney & Tremaine 2008) and the rotation curve of Eilers et al. (2019) in order to obtain a measurement of the pattern speed. With this we can also determine the radius of the CR.[3] We also document an abrupt change in the vertical structure of the galaxy very near to the OLR; we believe this speaks to north–south differences in the Galactic bar or perhaps some interaction between the OLR and separate north–south differences in the plane (Widrow et al. 2012; Yanny & Gardner 2013; Ferguson et al. 2017; Bennett & Bovy 2018). We note, for reference, that a significant north–south asymmetry has been recently suggested in the GC excess (Leane & Slatyer 2020). Finally, we compare our results with those already in the literature, as well as with other established features of the bar, noting the additional possibility of non-steady-state and/or axial-symmetry-breaking effects in the bar region.

2. Theory

As motivated through the perturbation theory analysis of Binney & Tremaine (2008) and depicted graphically in Dehnen (2000), the Galactic bar drives the OLR, holding sway over the shape of stellar orbits despite the affected stars not being within the physical extent of the bar, at Galactocentric, in-plane $R < \ell_{\rm bar}$, where $\ell_{\rm bar}$ is the bar half-length. Due to the periodic nature of the bar's gravitational force on stars at $R > \ell_{\rm bar}$, stars may receive a pull from the bar at the same phase in their orbit, exciting the orbit into an elliptical shape. For stars just inside (outside) the radius of the OLR, orbits are elongated perpendicular (parallel) to the bar (Contopoulos & Papayannopoulos 1980; Dehnen 2000), which has been thought to point at $\sim$10°–70° (Dehnen 2000) away from the Sun–GC line ($\phi = 180°$), with more recent work (Robin et al. 2012; Portail 2016; Anders et al. 2019) finding values within 13°–$\sim$40°.

Given that this effect has ϕ dependence, it breaks axial symmetry and thus can result in a measurably nonzero value of the axial asymmetry, $\mathcal{A}$, about the anticenter line as defined in Gardner et al. (2020). Indeed, one would expect that the stars "promoted" to higher R by the bar near the OLR would cause a very slight overdensity over a small range in azimuth near the bar's principal axis at some value $R_{\rm OLR} + \Delta R$ and leave behind a commensurate, slight underdensity at some $R_{\rm OLR}$–ΔR. By scanning over various values of R we have found that $\mathcal{A}$ varies radially (Hinkel et al. 2020).

The orbital alignments due to the central bar in the OLR region break axial asymmetry in the manner illustrated schematically in Figure 1. Just outside the resonant radius, we expect to find more stars to the right of the $\phi = 180°$ line ($\phi < 180°$), and expect to find more stars on the left ($\phi > 180°$) when just inside the resonant radius. Thus, as one moves outward in R the expected axial asymmetry would go from left-heavy to right-heavy, corresponding to a sign flip:

$$\mathcal{A}(R < R_{\rm OLR}) > 0 \longrightarrow \mathcal{A}(R > R_{\rm OLR}) < 0. \quad (1)$$

As such, the value of R that yields zero asymmetry is the location of the sign flip and thus the location of the OLR. In contrast, if the axially asymmetric effect were, rather, a CR, then the sense of the sign flip would change from $\mathcal{A} < 0 \longrightarrow \mathcal{A} > 0$ as R increases.

Following the methods of Binney & Tremaine (2008), a nonaxisymmetric contribution to the Galactic gravitational potential can be treated as a weak perturbation. Working in a reference frame rotating with the bar, at a steady pattern speed $\Omega_{\rm p}$, we have the Lagrangian

$$L = \frac{1}{2}\dot{R}^2 + \frac{1}{2}[R(\dot{\varphi} + \Omega_{\rm p})]^2 - \Phi(R, \varphi), \quad (2)$$

where we employ cylindrical coordinates with $\varphi = 0$ aligned along its long axis. The potential can be broken into an unperturbed, axisymmetric potential and a nonaxisymmetric correction:

$$\Phi(R, \varphi) = \Phi_{\rm u}(R) + \Phi_1(R, \varphi). \quad (3)$$

In the absence of the perturbation, we find a circular orbit at R with $\dot{\varphi} = \Omega - \Omega_{\rm p}$, where the frequency

$$\Omega = \pm\sqrt{\frac{1}{R}\frac{d\Phi_u}{dR}}, \quad (4)$$

where $\Omega > 0$ corresponds to prograde rotation. Specifying the form of the perturbing potential as per Binney & Tremaine (2008) we have

$$\Phi_1(R, \varphi) = \Phi_{\rm bar}(R)\cos(m\varphi), \quad (5)$$

where $m = 2$ for a Lindblad resonance. Now with $R(t) = R_{\rm u} + R_1(t)$ and $\varphi(t) = \varphi_{\rm u}\ (t) + \varphi_1(t)$, analyzing the equations of motion while working to leading order in

[3] Our analysis uses the rotation curve of Eilers et al. (2019), which assumes $R_0 = 8.122(31)$ kpc (Abuter et al. 2018), whereas we employ a subsequent (and more precise) determination of the Sun–GC distance, $R_0 = 8.178(26)$ kpc (Abuter et al. 2019) as appropriate.

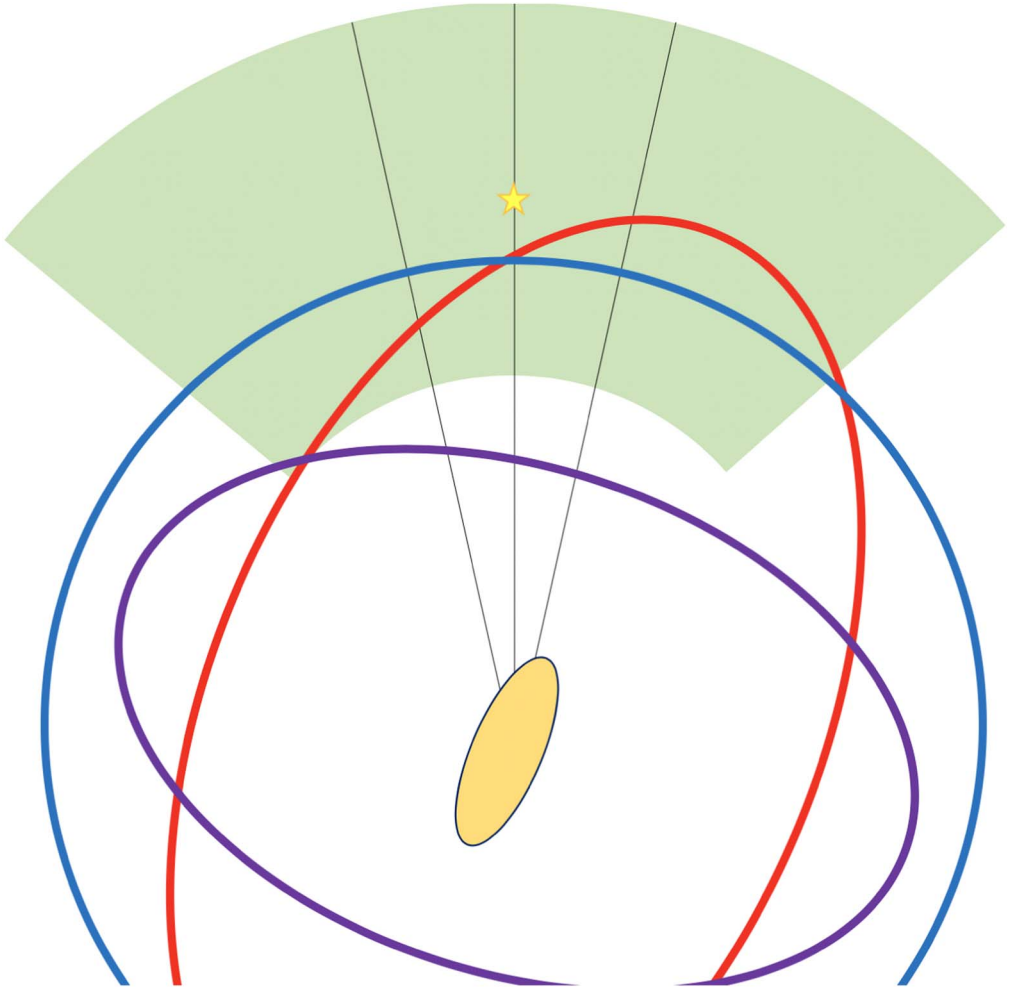

Figure 1. Schematic depiction of the orbital alignments due to the bar in the OLR region. The blue circle is the orbital radius of the OLR, the purple ellipse is an orbit interior to the OLR, and the red ellipse is an orbit exterior to the OLR. The green annular wedge region is our sample's in-plane footprint, with a star signifying the Sun's position, and the yellow ellipse is the Galactic bar. Stellar orbits tend to align parallel (perpendicular) to the bar when the orbit is just outside (inside) the outer Lindblad resonant radius. The geometry has been greatly exaggerated and we have shown closed orbits only, in order to illustrate the small effect we have found.

$|\Phi_l/\Phi_u| \ll 1$ and assuming $\varphi_l \ll \varphi_u$ yields

$$\ddot{R}_l + \kappa_0^2 R_l = -\left[\frac{d\Phi_{bar}}{dR} + \frac{2\Omega\Phi_{bar}}{R(\Omega - \Omega_p)}\right]_{R=R_u} \times \cos(m(\Omega(R_u) - \Omega_p)t), \quad (6)$$

where κ_0 is the natural harmonic frequency for the oscillatory perturbation provided by the bar,

$$\kappa_0^2 = \left(\frac{d^2\Phi_u}{dR^2} + 3\Omega^2\right)_{R=R_u} = \left(R\frac{d\Omega^2}{dR} + 4\Omega^2\right)_{R=R_u}, \quad (7)$$

and the general solution

$$R_l(t) = A\cos(\kappa_0 t + \alpha) - \left[\frac{d\Phi_{bar}}{dR} + \frac{2\Omega\Phi_{bar}}{R(\Omega - \Omega_p)}\right]_{R=R_u} \times \left(\frac{\cos(m(\Omega - \Omega_p)t)}{\kappa_0^2 - m^2(\Omega - \Omega_p)^2}\right), \quad (8)$$

so that open orbits appear with nonzero, arbitrary A for any α. Regardless, a resonance appears if $\kappa_0^2 - m^2(\Omega - \Omega_p)^2 = 0$, and it is an $m = 2$ OLR if

$$\Omega_p - \Omega = \kappa_0/2. \quad (9)$$

Notice this condition can be combined with Equation (7) to yield

$$4(\Omega_p - \Omega)^2|_{R=R_{OLR}} = \left(R\frac{d\Omega^2}{dR} + 4\Omega^2\right)_{R=R_{OLR}}, \quad (10)$$

to give the pattern speed from R_{OLR} and the R dependence of Ω:

$$\Omega_p = \Omega(R_{OLR}) + \frac{1}{2}\sqrt{4\Omega^2(R_{OLR}) + R_{OLR}\frac{d\Omega^2}{dR}\Big|_{R=R_{OLR}}}. \quad (11)$$

Finally, the pattern speed determines the CR radius:

$$\Omega_p = \Omega(R_{CR}), \quad (12)$$

noting that we cannot also determine the location of the ILR with these methods for want of information on Ω with R in the very inner portion of our Galaxy.

To determine the numerical value of the pattern speed and more, we use an observational assessment of the Galactic rotation curve, which yields both Ω^2 and $d\Omega^2/dR$ with R. That

is, the Galactic rotation curve is the circular speed v_c with R, where

$$\Omega \equiv \frac{v_c(R)}{R} = \sqrt{\frac{1}{R}\frac{d\Phi_u}{dR}}. \quad (13)$$

For this, we use the recent, high-precision determination of Eilers et al. (2019), which uses an analysis of red giant branch stars from Gaia DR2, cross-matched with APOGEE data, for refined distance assessments (Hogg et al. 2019). The analysis itself uses a Jeans equation framework in which the underlying Galactic distribution function $f(\boldsymbol{x}, \boldsymbol{v}, t)$ is assumed to be axially symmetric and in steady state. This yields

$$v_c^2 = \langle v_\phi \rangle^2 - \langle v_R \rangle^2 \left(1 + \frac{\partial \ln \langle v_R^2 \rangle}{\partial \ln R} + \frac{\partial \ln \nu}{\partial \ln R}\right) + \delta, \quad (14)$$

where $\nu(\boldsymbol{x}, t) = \int d^3\boldsymbol{v} f(\boldsymbol{x}, \boldsymbol{v}, t)$ and $\delta = 0$. We can, however, determine the modification of v_c^2 were all the neglected terms included. This gives

$$\delta = -R\frac{\partial}{\partial t}(\langle v_R \rangle \ln \nu) - \frac{\partial}{\partial \phi}(\langle v_R v_\phi \rangle \ln \nu) - R\frac{\partial}{\partial z}(\langle v_R v_z \rangle \ln \nu). \quad (15)$$

where the additions reflect corrections for non-steady-state, axial-symmetry-breaking, and z-dependent effects, respectively. The z-dependent term also appears in Eilers et al. (2019) and is estimated to affect v_c at the $\sim$1% level at $R \sim 18$ kpc. The axial-symmetry-breaking term vanishes if $\nu(\mathbf{x})$ itself is axially symmetric. We will note a possible role for these small terms, likely characterized in size by the non-steady-state term, later. Eilers et al. (2019) determine $v_c(R)$ over $5 \lesssim R \lesssim 25$ kpc, for which they report the linear parameterization

$$v_c(R) = (229.0 \pm 0.2)\,\mathrm{km\ s^{-1}} - (1.7 \pm 0.1)\,\mathrm{km\ s^{-1}\ kpc^{-1}} \cdot (R - R_0), \quad (16)$$

where $R_0 = 8.122(31)$ kpc (Abuter et al. 2018) has been employed. We employ this parameterization in what follows.

3. Analysis

As we showed in Gardner et al. (2020), effects from the LMC and Galactic bar are the two dominant contributors of axial-symmetry breaking in the solar neighborhood. Further, in Hinkel et al. (2020), we found a sign flip in the sense of the asymmetry that matches that expected from an OLR assuming the determined bar orientation (Robin et al. 2012; Portail 2016; Anders et al. 2019) does indeed point in the third quadrant of the galactocentric rectangular coordinate system in which the positive x-axis points from the GC in the direction opposite the Sun with y and z following from a right-hand coordinate system choice in which z increases from zero at the midplane to larger values toward the North Galactic Pole. Here, we refine the sign-flip analysis in order to remove any background effects from the overall distortion of the Galaxy due to the LMC's influence, which we found to be described by a prolate shape pointing toward the LMC (Erkal et al. 2019; Gardner et al. 2020). We expect this global background effect to be a constant offset over the volume of space we study, and we define this background asymmetry as $\langle \mathcal{A} \rangle_B$. As such, the precise value of R where the equality

$$\langle \mathcal{A}(R) \rangle - \langle \mathcal{A} \rangle_B = 0 \quad (17)$$

corresponds to the radius of the OLR. We estimate the background asymmetry by integrating over the entire volume of the sample of Gardner et al. (2020) and find that $\langle \mathcal{A} \rangle_B = -0.0032 \pm 0.0003$. This moves our measurement of the sign flip from Hinkel et al. (2020), and thus R_{OLR}, slightly outward in R, as expected.

In practice, we repeat the radial scans of Hinkel et al. (2020) and subtract the offset in order to find the bin with zero asymmetry. The results of this analysis are tabulated in Table 1. The OLR radius is defined as the center of the bin in Table 1, which, after accounting for the background asymmetry, yields an asymmetry that is within 1σ from 0. Note that, after rounding, this yields $R_{OLR} = (0.96 \pm 0.03)R_0 = 7.85 \pm 0.25$ kpc where the uncertainty in the OLR radius assessment is the first ΔR in the successively smaller ΔR scans in which a "zero" is no longer discernible in just a single bin, rounded to one significant figure. The measured axial asymmetry just within and beyond the determined OLR location in R is shown in Figure 2. We discuss its interesting north/south differences in the next section. Here we wish to focus on the size of the asymmetry $\langle \mathcal{A}(R) \rangle - \langle \mathcal{A} \rangle_B$ itself because this is reflective of the number of stars that populate the distorted orbits we have analyzed. As tabulated in Table 2, the flip in sign of the asymmetry is quite symmetric about the outer Lindblad resonant radius, which is expected if the stars are excited to higher R and leave behind a dearth of stars at lower R. Additionally, Table 2 suggests that $\mathcal{O}(10^4)$ stars populate the distorted orbits that we analyze, corresponding to a small but statistically significant change in the sign of the asymmetry We report our final value of the determined OLR location in Table 3.

Table 1
Axial Asymmetries, N+S, Averaged over Azimuthal Angles

R_i–R_f (R_0)	ΔR (R_0)	$\langle \mathcal{A}(\phi) \rangle - \langle \mathcal{A} \rangle_B$	$\sigma_{\langle \mathcal{A} \rangle}$	Sign
0.8750-0.9375	0.0625	+0.0103	0.0015	+
0.9000-0.9625	0.0625	+0.0067	0.0014	+
0.9250-0.9875	0.0625	+0.0005	0.0014	0
0.9250-0.9625	0.0375	+0.0049	0.0015	+
0.9375-0.9750	0.0375	+0.0009	0.0015	0
0.9500-0.9875	0.0375	−0.0031	0.0014	−
0.9375-0.9625	0.0250	+0.0037	0.0016	+
0.9438-0.9688	0.0250	+0.0013	0.0015	0
0.9500-0.9750	0.0250	−0.0015	0.0015	0

Note. We compute each asymmetry in a wedge of size ΔR averaged over azimuthal angles about the anticenter direction out to $|180-\phi|=6$. The radial bin begins at R_i and is moved outward for each iteration. We refine the location of the sign flip iteratively by computing the average asymmetry with R_i for smaller ΔR. Note that the distances are in units of R_0 and that the "Sign" is assessed by whether the magnitude of the asymmetry difference is in excess of its error. The uncertainty in the final asymmetry $\sigma_{\langle \mathcal{A} \rangle}$ has been computed by adding the systematic axial asymmetry of Hinkel et al. (2020) and statistical errors in quadrature and then adding the uncertainty from the background subtraction.

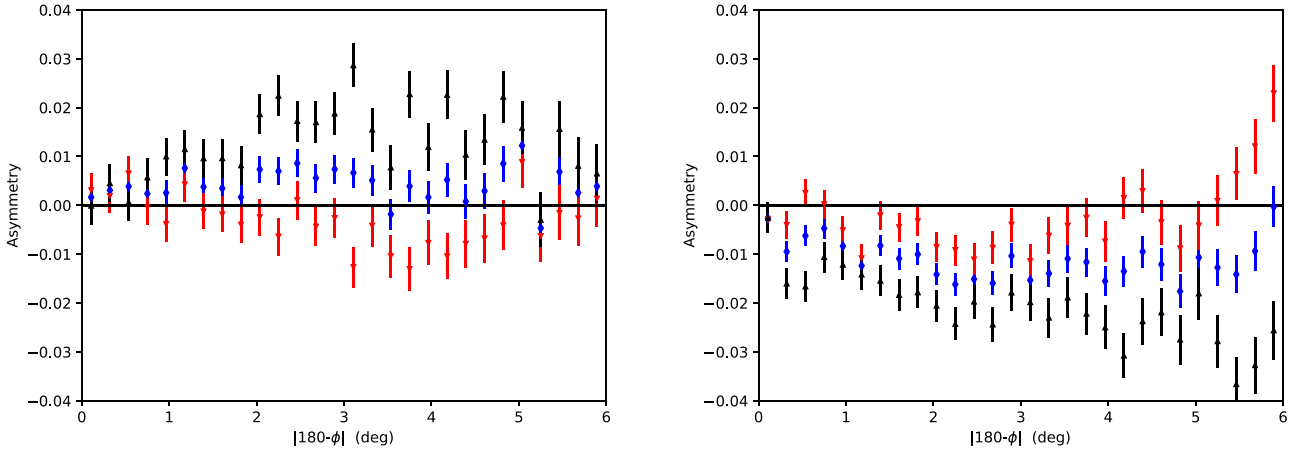

Figure 2. (a) Axial asymmetry for $R \in [0.8975, 0.9600]R_0$. (b) Axial asymmetry for $R \in [0.9600, 1.0225]R_0$. The blue diamonds are the aggregate axial asymmetry, and the black and red triangles are for the northern ($z > 0$) and southern ($z < 0$) halves, respectively. The sign flip in the aggregate asymmetry is clearly visible here, which we attribute to the bar's OLR. In addition, the vertical structure changes just beyond the OLR, with a north–left correlation for $R < R_{\rm OLR}$ and a north–right correlation for $R > R_{\rm OLR}$.

Table 2
Star Counts and Background-corrected Axial Asymmetries for Bins of Varying Width, ΔR, Probing Just Interior and Exterior to the Outer Lindblad Resonant Radius

ΔR (R_0)	N ($[R_{\rm OLR}$–ΔR, $R_{\rm OLR}]$)	$N([R_{\rm OLR}, R_{\rm OLR} + \Delta R])$	$\mathcal{A}(R < R_{\rm OLR})$	$\mathcal{A}(R > R_{\rm OLR})$
0.0625	3,070,836	4,241,269	+0.0075(14)	−0.0076(14)
0.0500	2,615,604	3,383,670	+0.0068(14)	−0.0065(14)
0.0375	2,087,432	2,524,189	+0.0058(15)	−0.0050(14)
0.0250	1,478,859	1,738,446	+0.0050(16)	−0.0047(15)

Note. As we focus in on the OLR, the magnitude of the asymmetry becomes slightly smaller, perhaps suggesting the magnitude of the first order radial correction, $|R_1|$, (see Equation (8)) can be larger than a couple hundred parsecs. Also note that the radial bin external to the OLR has more stars due to the geometry of our stellar sample (Gardner et al. 2020; Hinkel et al. 2020) and the uncertainty in each asymmetry is indicated in parentheses.

Table 3
The Literature Offers a Wide Array of Pattern Speed Assessments

Source	$\Omega_{\rm p}$ (km s^{-1} kpc^{-1})	Estimate of $R_{\rm CR}$ (kpc)	Estimate of $R_{\rm OLR}$ (kpc)
Dehnen (1999)	53 ± 3	4.44	7.34
Sanders et al. (2019)	41 ± 3	5.69	9.32
Sanders et al. (2019)[a]	31 ± 1	7.43	12.01
Hunt & Bovy (2018) ($m = 4$)	$\lesssim 1.35\Omega_0$[b]	>6.15	>10.04
Portail et al. (2015)	25–30	7.66–9.10	12.37–14.54
Portail et al. (2017)	39.0 ± 3.5	5.97	9.75
Monari et al. (2017)	$>1.8\Omega_0$	<4.66	<7.69
Chakrabarty (2007)	$57.4^{+2.8}_{-3.3}$	4.11	6.81
This work (without LMC correction)	49.9 ± 2.2	4.71 ± 0.26	7.77 ± 0.25
This work (with LMC correction)	49.3 ± 2.2	4.76 ± 0.27	7.85 ± 0.25
Bland-Hawthorn & Gerhard (2016)[c]	43 ± 9	5.43	8.91

Notes. The various determinations use differing assessments in the Sun–GC distance and the local rotation curve, which could result in small changes. Also, to report our harmonized CR and OLR estimates for each work we have used the rotation curve of Eilers et al. (2019) and the Sun–GC distance of Abuter et al. (2019).
[a] Includes data from the far side of the bar.
[b] $\Omega_0 \approx 28$ km s^{-1} kpc^{-1} is the rotational frequency at the solar circle.
[c] Approximate literature range adopted in a review of Galactic properties.

4. Results

In this analysis, we have chosen the rotation curve of Eilers et al. (2019) as it represents the only highly precise assessment of the Galaxy's rotation curve in the region of $5 \lesssim R \lesssim 25$ kpc. As a check, we compute the Oort constants, A and B, using the $v_c(R)$ parameterization in Equation (16) as given in Eilers et al. (2019) and find that $A = 14.95 \pm 0.43\,\mathrm{km\,s^{-1}\,kpc^{-1}}$ and $B = -13.25 \pm 0.43\,\mathrm{km\,s^{-1}\,kpc^{-1}}$, where we have combined the statistical and $\pm 3\%$ systematic error in quadrature. These numbers are in very good agreement with the recent findings of Li et al. (2019) using Gaia DR2 data within 500 pc of the Sun: $A = 15.1 \pm 0.1\,\mathrm{km\,s^{-1}\,kpc^{-1}}$ and $B = -13.4 \pm 0.1\,\mathrm{km\,s^{-1}\,kpc^{-1}}$, though there is some tension in the determination of B with respect to the earlier results of Binney & Tremaine (2008; $B = -12.4 \pm 0.6\,\mathrm{km\,s^{-1}\,kpc^{-1}}$) and Bovy (2017; $B = -11.9 \pm 0.4\,\mathrm{km\,s^{-1}\,kpc^{-1}}$).

This rotation curve, along with a precise measurement of the Sun–GC distance (Abuter et al. 2019) affords us the opportunity to use our OLR location determination to determine Ω_p and also the location of the CR. Employing Equation (11), we have $\Omega_p = 49.3 \pm 2.2\,\mathrm{km\,s^{-1}\,kpc^{-1}}$. By using our determined value of R_{OLR} and leading-order perturbation theory as per Binney & Tremaine (2008), our pattern speed determination does not depend on any assumptions about the bar potential, other than its interpretation as a $m = 2$ resonance. Moreover, the pattern speed we find falls within the literature average given by Bland-Hawthorn & Gerhard (2016), though it tends to be on the higher end as shown among a sample of other findings in Table 3. We recall, though, that as in the case of Sanders et al. (2019), the pattern speed estimates can be biased low when including observations beyond the GC.

Using this determined pattern speed in Equation (12), we estimate $R_{\mathrm{CR}} = (0.58 \pm 0.04)\,R_0 = 4.76 \pm 0.27$ kpc. Interestingly we determine that $R_{\mathrm{OLR}}/R_{\mathrm{CR}} \approx 1.7$ in agreement with the expectation of Dehnen (2000) if the bar is weak and the rotation curve is flat. This is a useful consistency check as our CR determination is just compatible (within 1σ) with the lower R limit of the Eilers et al. (2019) range of validity. Additionally, this corotation estimate is also just compatible within errors with the half-length of the bar, for which Wegg et al. (2015) find $\ell_{\mathrm{bar}} = 5.0 \pm 0.2$ kpc. We note that a weak bar should possess a CR at radii beyond the half-length of the bar (Aguerri et al. 1998). If the parameter δ is positive, reflective of a driving effect from a slowing of the bar (Weinberg 1994; Chiba et al. 2019), then we can bring the picture into better agreement. The fluctuation of the bar's parameters suggested by Hilmi et al. (2020) could explain the non-steady-state effects we infer.

Given the diverse array of pattern speeds in the literature, as compiled in Table 3, it should perhaps come as no surprise that both the CR and the OLR have been argued to be near the solar circle. As such, the wide spread in pattern speed assessments inevitably means that there are correspondingly large ranges for R_{CR} and R_{OLR}. Interestingly, though, a recent measurement of R_{OLR} by Khoperskov et al. (2020) estimates the location of the OLR without assuming a pattern speed. They find that the OLR is near $R = 9$ kpc, though they rely on models that draw random distributions of Gaia data that are very close to the midplane, for which the effects of reddening and extinction from dust would seem to be important. As an additional effect, the Milky Way's spiral arms break axial symmetry, but we have taken care to ensure that our sample is sufficiently out of plane so as to minimize any confounding effects due to spiral structure (Gardner et al. 2020).

Finally, in addition to the pattern speed and the locations of the OLR and CR, we have found an unexpected, abrupt change in vertical structure near the OLR. By computing the axial asymmetry for $z > 0$ and $z < 0$, henceforth the north (N) and south (S) respectively, we find as R increases through the OLR, the asymmetry in the N goes from left-heavy to right-heavy, with a smaller effect of opposite sense in the S, as illustrated in Figure 2. Speculatively, this could be due to a vertical resonance with the bar, a bar tilted slightly out of plane, or perhaps stem from a N/S asymmetry in the bar itself, where we note that a N/S effect has been found in the GC excess (Leane & Slatyer 2020). Alternatively, local N/S differences have been noted in the solar neighborhood and have been attributed to the Sagittarius impact (Widrow et al. 2012; Yanny & Gardner 2013; Ferguson et al. 2017), so that the vertical effects seen near the OLR may come from a completely separate event. Indeed, Carrillo et al. (2019) have suggested that the Sagittarius impact could have significantly perturbed the Galactic bar, or could have even been responsible for its genesis. Detailed studies of the Galactic bar resonances in the presence of small vertical asymmetries in the bar or in the local disk, or subject to significant vertical perturbations could conceivably help explain this behavior.

We note that our assumption of an $m = 2$ OLR resonance can be tested through additional observational studies. An $m = 2$ OLR resonance implies axially asymmetric structures at $\phi = 0°$, $180°$, but the possibility of an $m = 4$ (Hunt & Bovy 2018) OLR implies asymmetric structures at $\phi = 90°$, $270°$ also, so that over the longer term there is another observational test (Hunt & Bovy 2018). Yet, this is not the only possibility. Note that the existence of an $m = 4$ resonance would imply that an $m = 2$ resonance could appear (if it exists) at larger R as well, so that if our sign flip were interpreted as an $m = 4$ resonance, we would find $\Omega_p \approx 39.3\,\mathrm{km\,s^{-1}\,kpc^{-1}}$ and an $m = 2$ resonance at $R_{\mathrm{OLR}} \approx 11.6$ kpc. This alternative possibility meshes well with the findings of Portail et al. (2017) and could be explored in future data releases.

5. Summary

We have shown that axial-symmetry-breaking orbital alignments are detectable at very small levels and that our analysis of this effect is consistent with leading-order perturbation theory that models the Galactic bar as a weakly nonaxially symmetric effect. Through this approach, we avoid the need to assume a form for the Galaxy's potential, apart from the assumption of an $m = 2$ potential, and we only rely on the quadrant in which the bar points in order to interpret the sign flip we observe in the asymmetry. We have found that the OLR is situated at $R_{\mathrm{OLR}} = 7.85 \pm 0.25$ kpc, which implies the pattern speed of the bar is $\Omega_p = 49.3 \pm 2.2\,\mathrm{km\,s^{-1}\,kpc^{-1}}$, and thus the radius of corotation is $R_{\mathrm{CR}} = 4.76 \pm 0.27$ kpc. Additionally, we find evidence for a change in the vertical structure of the disk near the OLR, but we cannot resolve if this effect is due to a possibly tilted or asymmetric bar, or if the effect is local in nature, possibly due to the Sagittarius impact. Our approach is entirely novel, but our estimates for the pattern speed of the bar are very much consistent with the upward revision of the Ω_p of Sanders et al. (2019) and Bovy et al.

(2019) as suggested by the work of Hilmi et al. (2020), and our inferred resonance locations for the CR and the OLR are in remarkable agreement with the picture of Dehnen (1999), even if our assessments are much more precise. Thus we believe that our results are in support of a Galactic bar that is both weak and fast.

A.H. thanks the Universities Research Association for travel to Fermilab, the GAANN Fellowship for support, and Isaac Shlosman for discussion of the resonances of the Galactic bar. S.G. and A.H. acknowledge partial support from the U.S. Department of Energy under contract DE-FG02-96ER40989, and S.G. also acknowledges the University Research Professor fund of the University of Kentucky for partial support. The authors also thank the anonymous referee for helpful comments.

This document was prepared in part using the resources of Fermi National Accelerator Laboratory (Fermilab), a U.S. Department of Energy, Office of Science, HEP User Facility. Fermilab is managed by the Fermi Research Alliance, LLC (FRA), acting under Contract No. DE-AC02-07CH11359.

This work has made use of data from the European Space Agency (ESA) mission Gaia (https://www.cosmos.esa.int/gaia), processed by the Gaia Data Processing and Analysis Consortium (DPAC, https://www.cosmos.esa.int/web/gaia/dpac/consortium). Funding for the DPAC has been provided by national institutions, in particular the institutions participating in the Gaia Multilateral Agreement.

ORCID iDs

Austin Hinkel https://orcid.org/0000-0002-9785-914X
Susan Gardner https://orcid.org/0000-0002-6166-5546
Brian Yanny https://orcid.org/0000-0002-9541-2678

References

Abuter, R., Amorim, A., Anugu, N., et al. 2018, A&A, 615, L15
Abuter, R., Amorim, A., Bauböck, M., et al. 2019, A&A, 625, L10
Aguerri, J., Beckman, J., & Prieto, M. 1998, AJ, 116, 2136
Anders, F., Khalatyan, A., Chiappini, C., et al. 2019, A&A, 628, A94
Antoja, T., Helmi, A., Dehnen, W., et al. 2014, A&A, 563, A60
Bennett, M., & Bovy, J. 2018, MNRAS, 482, 1417
Binney, J., & Tremaine, S. 2008, Galactic Dynamics (Princeton, NJ: Princeton Univ. Press)
Bland-Hawthorn, J., & Gerhard, O. 2016, ARA&A, 54, 529
Bovy, J. 2017, MNRAS, 468, L63
Bovy, J., Leung, H. W., Hunt, J. A., et al. 2019, MNRAS, 490, 4740
Brown, A., Vallenari, A., Prusti, T., et al. 2018, A&A, 616, A1
Carrillo, I., Minchev, I., Steinmetz, M., et al. 2019, MNRAS, 490, 797
Chakrabarty, D. 2007, A&A, 467, 145
Chiba, R., Friske, J. K., & Schönrich, R. 2019, arXiv:1912.04304
Contopoulos, G., & Papayannopoulos, T. 1980, A&A, 92, 33
Debattista, V. P., Gerhard, O., & Sevenster, M. N. 2002, MNRAS, 334, 355
Dehnen, W. 1999, ApJL, 524, L35
Dehnen, W. 2000, AJ, 119, 800
Eilers, A.-C., Hogg, D. W., Rix, H.-W., & Ness, M. K. 2019, ApJ, 871, 120
Englmaier, P., & Gerhard, O. 1999, MNRAS, 304, 512
Erkal, D., Belokurov, V., Laporte, C., et al. 2019, MNRAS, 487, 2685
Ferguson, D., Gardner, S., & Yanny, B. 2017, ApJ, 843, 141
Fux, R. 2001, A&A, 373, 511
Gardner, S., Hinkel, A., & Yanny, B. 2020, ApJ, 890, 110
Gerhard, O., & Wegg, C. 2015, in Lessons from the Local Group, ed. K. Freeman et al. (Cham: Springer), 43
Hilmi, T., Minchev, I., Martig, M., et al. 2020, MNRAS, 497, 933
Hinkel, A., Gardner, S., & Yanny, B. 2020, ApJ, 893, 105
Hogg, D. W., Eilers, A.-C., & Rix, H.-W. 2019, AJ, 158, 147
Hunt, J. A., & Bovy, J. 2018, MNRAS, 477, 3945
Khoperskov, S., Gerhard, O., Di Matteo, P., et al. 2020, A&A, 634, L8
Leane, R. K., & Slatyer, T. R. 2020, arXiv:2002.12371
Li, C., Zhao, G., & Yang, C. 2019, ApJ, 872, 205
Lindegren, L., Hernandez, J., Bombrun, A., et al. 2018, A&A, 616, A2
Minchev, I., Nordhaus, J., & Quillen, A. 2007, ApJL, 664, L31
Minniti, D., Lucas, P. W., Emerson, J. P., et al. 2010, NewA, 15, 433
Mishurov, Y. N., & Zenina, I. 1999, A&A, 341, 81
Monari, G., Kawata, D., Hunt, J. A., & Famaey, B. 2017, MNRAS, 466, L113
Portail, M. 2016, PhD thesis, LMU München: Fakultät für Physik
Portail, M., Gerhard, O., Wegg, C., & Ness, M. 2017, MNRAS, 465, 1621
Portail, M., Wegg, C., Gerhard, O., & Martinez-Valpuesta, I. 2015, MNRAS, 448, 713
Prusti, T., De Bruijne, J., Brown, A. G., et al. 2016, A&A, 595, A1
Raboud, D., Grenon, M., Martinet, L., Fux, R., & Udry, S. 1998, A&A, 335, L61
Robin, A. C., Marshall, D. J., Schultheis, M., & Reylé, C. 2012, A&A, 538, A106
Sanders, J. L., Smith, L., & Evans, N. W. 2019, MNRAS, 488, 4552
Sellwood, J. 2010, MNRAS, 409, 145
Tremaine, S., & Weinberg, M. 1984, ApJL, 282, L5
Wegg, C., Gerhard, O., & Portail, M. 2015, MNRAS, 450, 4050
Weinberg, M. D. 1994, ApJ, 420, 597
Widrow, L. M., Gardner, S., Yanny, B., Dodelson, S., & Chen, H.-Y. 2012, ApJL, 750, L41
Yanny, B., & Gardner, S. 2013, ApJ, 777, 91